

Characteristics of Branched Flows of High-Current Relativistic Electron Beams in Porous Materials

K. Jiang,¹ T. W. Huang,^{1, a)} R. Li,¹ and C. T. Zhou^{1, b)}

Shenzhen Key Laboratory of Ultraintense Laser and Advanced Material Technology,
Center for Advanced Material Diagnostic Technology, and College of Engineering Physics,
Shenzhen Technology University, Shenzhen 518118, People's Republic of China

(Dated: 18 December 2023)

Branched flow is a universal phenomenon in which treebranch-like filaments form through traveling waves or particle flows in irregular mediums. Branched flow of high-current relativistic electron beams (REBs) has been recently discovered [Phys. Rev. Lett. **130**, 185001 (2023)]. It exhibits unique features, including remarkably high beam density at predictable caustic locations, efficient energy coupling between the beam and background medium, etc. This paper presents investigations on REB branching, focusing on the influence of interaction parameters on branching patterns and providing detailed analyses of the dynamics of individual beam electrons. The insights gained contribute to a nuanced understanding of the intricate nature of REB branching and its potential applications in the future.

I. INTRODUCTION

Branched flow refers to a phenomenon wherein treebranch-like filaments emerge as waves or particle flows propagate through an irregular medium¹. The medium's irregularity manifests through an effective potential V , which is randomly uneven, spatially smooth, weak ($V_{\text{rms}} \ll E_k$, where E_k represents the kinetic energy of the traveling flow), and long-range correlated (with a correlation length l_c exceeding the flow wavelength)²⁻⁴. In such conditions, sudden and significant momentum changes in the flow are absent, but accumulated small changes profoundly influence the morphologies and dynamics of the flow. In particular, caustics and filaments form as the flow undergoes bending and bundling at favorable locations. For example, instead of smoothly spreading, tsunami waves refract and form branching strands due to fluctuations in the ocean height⁵. Impurities within semiconductors can induce branched flows of current-carrying electrons⁶. Cosmic rays form branches when traversing inhomogeneous interstellar dust clouds⁷. Light undergoes branched flow in complex media characterized by refractive index fluctuations⁸⁻¹⁰.

Recently, we reported that high-current relativistic electron beam (REB) propagation in porous materials (e.g., foam) can cascade into thin and dense branches at a length scale d_0 given by

$$d_0 \propto l_c^{-1/3} n_{b0}^{-2/3} \gamma^{2/3}, \quad (1)$$

thereby bringing the branched flow phenomenon to high-energy-density physics¹¹. Here l_c is the average pore size of the foam, n_{b0} and γ denote the initial density and Lorentz factor of the REB, respectively. Notably,

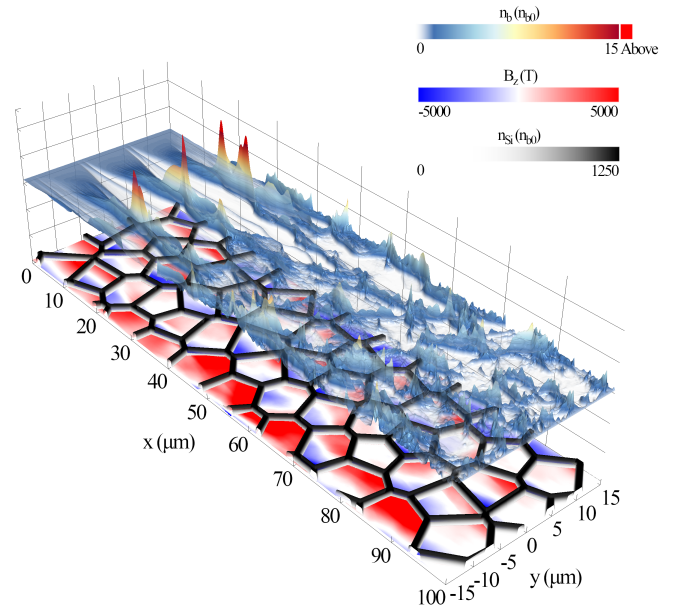


FIG. 1. Formation of branched flow patterns as a high-current relativistic electron beam propagates through a porous SiO₂ foam along the x direction. The red to blue color bar is for the beam density (in units of n_{b0} , same below) at $t = 333$ fs. The initial density distribution of Si atoms in the foam (black) and self-generated azimuthal magnetic field B_z (red and blue, in tesla) at $t = 333$ fs are shown beneath the beam density.

REB branching differs from beam-plasma instabilities, as it arises from the microscopic skeleton-and-pore heterogeneity of the foam. The compensating return current, located within skin layers of the skeletons, induces magnetic fields in the unevenly distributed pores. As a consequence, the beam electrons undergo successive scattering by these fields, leading to branched flow. Furthermore, REB branching is accompanied by a significant increase in beam-target energy coupling efficiency, which can be two orders of magnitude larger than that in homogeneous plasmas with similar average

^{a)} Electronic mail: taiwu.huang@sztu.edu.cn

^{b)} Electronic mail: zcangtao@sztu.edu.cn

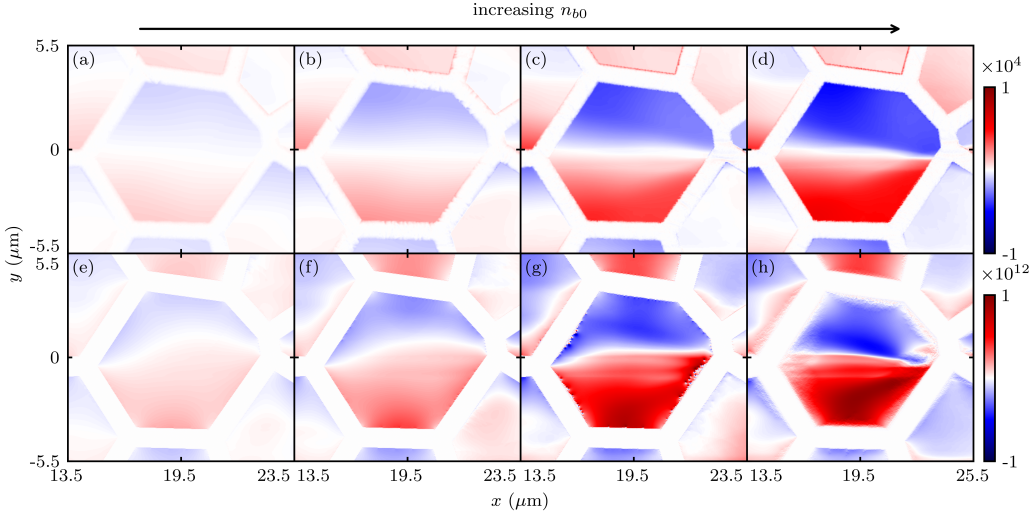


FIG. 2. From top to bottom, distributions of azimuthal magnetic field B_z (in tesla) and transverse electric field E_y (in V/m) in a selected region. From left to right, the initial density of the electron beam $n_{b0} = 3.44 \times 10^{24}$, 6.88×10^{24} , 1.376×10^{24} , and $1.72 \times 10^{25} \text{ m}^{-3}$. In all the cases, l_c keeps at $8 \text{ } \mu\text{m}$.

density.

In this paper, we present a comprehensive investigation into the branched flow of REBs, focusing on two aspects: (1) the impact of beam and foam parameters on the branching patterns, and (2) the dynamics of individual beam electrons. The paper is organized as follows: Section II introduces pore-resolved particle-in-cell (PIC) simulations, providing detailed results on the branched flow pattern. Since the branched flow pattern is determined by self-generated fields, Sect. III delves into the discussion on how REB and foam parameters affect these fields. Section IV presents the influence of interaction parameters on the branched flow pattern. In Sect. V, we present detailed analyses of the dynamics of individual beam electrons. The paper concludes with discussions in Sect. VI.

II. PORE-RESOLVED PARTICLE-IN-CELL SIMULATION AND RESULTS

In early simulations regarding REB transport in foam, the foam is usually simplified as a homogeneous continuum with a volumetric average density^{12–16}. That is, the foam's possible fine structuring is neglected. A likely reason for the assumption is that the foam considered is rather dense, such that its internal structure is smaller than the spatial scale of interest. Another reason might be the computational limitations at that time, which may have hindered the resolution of such fine structures. While results from the continuum assumption agree reasonably well with experiments using dense foam, this assumption proves inadequate for low-density foams characterized by spongelike submicron-sized intertwining solid-density skeletons with micron-sized empty pores in between¹⁷. These microstructures can significantly affect

macroscopic results, necessitating their consideration in simulations^{18–25}.

To elucidate the impact of these microstructures on the propagation of REBs, we perform pore-resolved two-dimensional (2D) PIC simulations using the EPOCH code²⁶. As shown in Fig. 1, in the simulation, the porous material is SiO_2 foam. The foam's internal structures are modeled by random Voronoi cells²⁷. For definitiveness, the skeleton thickness $l_d = 1 \text{ } \mu\text{m}$ and average pore size $l_c = 8 \text{ } \mu\text{m}$. The skeletons consist of solid-density Si and O atoms, with respective densities of $n_{\text{Si}} = 2.15 \times 10^{28} \text{ m}^{-3}$ and $n_{\text{O}} = 4.3 \times 10^{28} \text{ m}^{-3}$. For simplicity, the initial REB is monoenergetic and of uniform density $n_{b0} = 1.72 \times 10^{25} \text{ m}^{-3}$, with a duration of 400 fs and Lorentz factor $\gamma = 100$. Detailed discussions regarding the impact of foam and REB parameters will follow. The simulation box spans from $0 \text{ } \mu\text{m} < x < 100 \text{ } \mu\text{m}$ and $-15 \text{ } \mu\text{m} < y < 15 \text{ } \mu\text{m}$. To resolve the skin depth of the solid skeletons, the spatial resolution $\Delta = 12.5 \text{ nm}$. There are 14 macroparticles per cell for both Si and O atoms and 100 for the beam electrons. In addition, over 300 macroelectrons per cell can be produced from the skeletons by field ionization. Periodic boundaries are used in the transverse direction. As discussed in Ref. [11], collisions are deemed negligible and are not included here.

As shown in Fig. 1, REB propagation in the foam induces uneven fields in the pores. The latter, in turn, deflects the beam electrons, resulting in REB branching. Specifically, the REB breaks up into three narrow dense branches. These branches subsequently broaden, intersect, and evolve into a fluctuating pattern. Since the Lorentz force associated with the azimuthal magnetic field B_z is twice as large as that from electric fields (see discussion later and Ref. [11]), B_z is more influential in shaping the dynamics of beam electrons. To

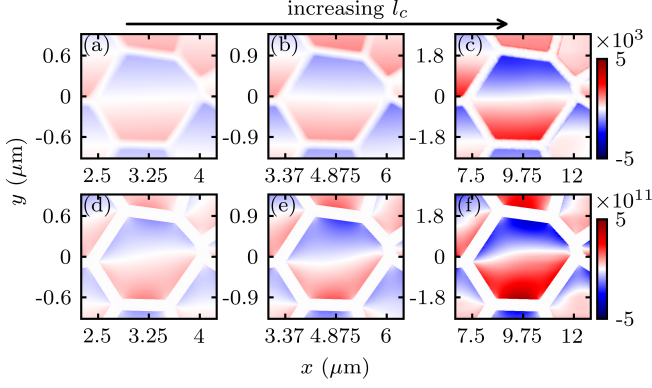


FIG. 3. From top to bottom, distributions of azimuthal magnetic field B_z (in tesla) and transverse electric field E_y (in V/m). From left to right, the average pore size of the foam $l_c = 1.33, 2, 4$, and $8 \mu\text{m}$.

visualize the electron motion, one may neglect the effects of electric fields and focus on the deflection caused by B_z for simplicity. The gyroradius of beam electrons, given by $r_g = \gamma m_e c / e B_z \sim 41.6 \mu\text{m}$, is significantly larger than the average pore size (or the characteristic length scale of B_z) of $l_c = 8 \mu\text{m}$. Here m_e and $-e$ are the electron rest mass and charge, and c is the vacuum light speed. Therefore, the electrons can travel over several pores before significant deflection occurs.

Considering the REB dynamics from an energy perspective may provide additional insights. The effective potential strength of the uneven fields is expressed as $V_{\text{rms}} \sim \mu_0 e^2 c^2 l_c^2 n_{b0} / 8\sqrt{3}^{11}$, and the initial kinetic energy of the beam electron reads $E_{k,b0} = \gamma m_e c^2$. Here, μ_0 is the vacuum permeability. The ratio $V_{\text{rms}} / E_{k,b0} \sim 0.03 \ll 1$, indicating that the magnitude of the effective potential is sufficiently small to cause only forward scatterings of the REB. These weak scatterings over several peaks and valleys of the potential V lead to the formation of branched flows. This process is characterized by seemingly random, time-irreversible behavior, yet it exhibits deterministic and predictable tendencies. Since the distribution of pores, along with the associated effective potential, is isotropic, the transverse separations between two adjacent caustics are almost the same and match well with l_c . Therefore, branched flow of REBs presents a new regime of beam-plasma interaction with typical features of complex systems, where patterns emerge from random yet correlated interactions.

III. SELF-GENERATED PORE FIELDS

Given that the self-generated pore fields B_z and E_y result in REB branching, this section considers the influence of interaction parameters on B_z and E_y . As discussed in Ref. [11], B_z arises from current

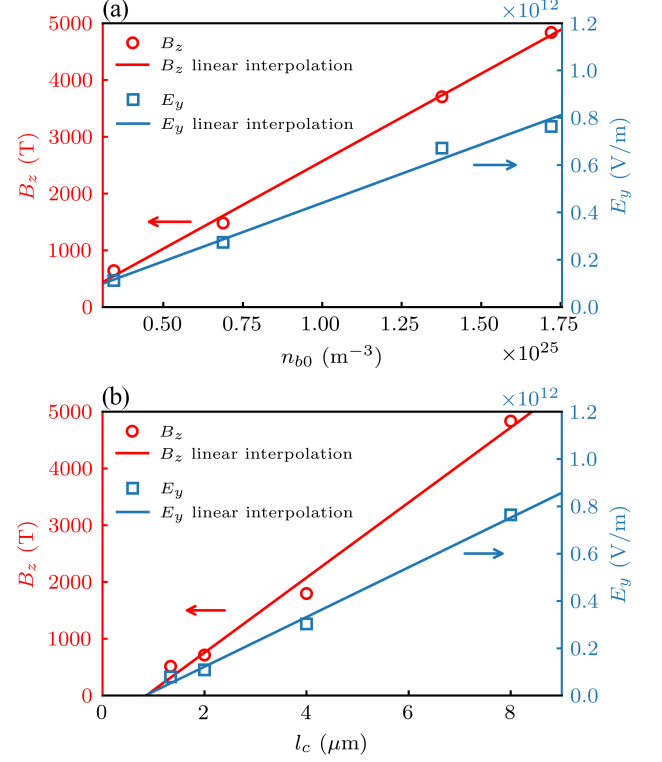


FIG. 4. (a) Strengths of the azimuthal magnetic field B_z (red circles) and transverse electric field E_y (blue squares) at $x = 20 \mu\text{m}$ and $y = -3 \mu\text{m}$ obtained from simulations for different initial beam density n_{b0} with $l_c = 8 \mu\text{m}$. (b) Same as (a), but at $x = 20l_c/8$ and $y = -3l_c/8$ obtained from simulations with different l_c . The solid lines are linear interpolations based on the simulation results.

neutralization. The return current, induced within skin layers of skeletons, are of huge density several times larger than the beam current, namely $j_r \sim |j_{b0}| l_c / 2l_s \exp(1)$. Here j_{b0} is the beam-current density, and l_s is the skin length of the skeletons. Since the solid-density skeletons effectively shield fields outside skin layers, the magnetic field induced by the current is distributed in the vacuum pores. The beam and return currents contribute approximately equally to the magnetic field, with the total magnetic strength given by Ampère's law as $|B_z| \sim \mu_0 e n_{b0} l_c c / 2 \propto n_{b0} l_c$. In addition, the REB, being a bunch of electrons, provides the space charge for the electrostatic fields E_y in the pore regions. From Poisson's equation one obtains $E_y \sim e n_{b0} l_c / 4\epsilon_0 \propto n_{b0} l_c$. As both B_z and E_y originate from the REB itself, the time scale for their onset is $\sim l_c / c$ (several femtoseconds), much shorter than the expansion time scale of the skeletons. The magnetic field B_z plays a more crucial role in scattering beam electrons ($|F_y| = e(c|B_z| - |E_y|) \sim ec|B_z|/2$), as the electrostatic and magnetic forces associated with the beam tend to cancel each other, leaving the net magnetic force provided by the return current to scatter the beam electrons.

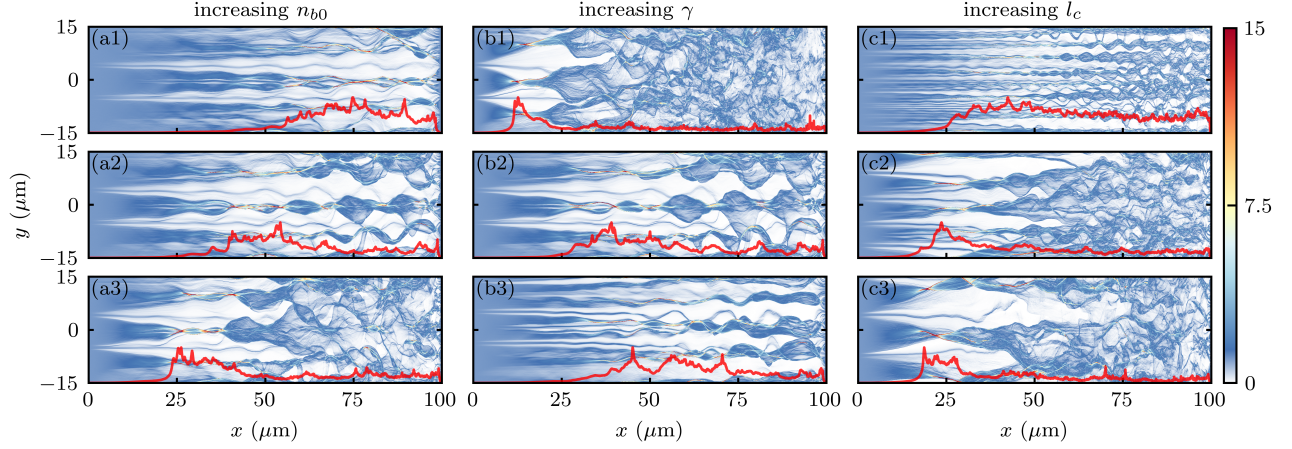


FIG. 5. Branched flow patterns (in unites of n_{b0} , same below) for (a1)-(a3) different initial beam densities at $n_{b0} = 3.44 \times 10^{24}$, 6.88×10^{24} , and $1.38 \times 10^{25} \text{ m}^{-3}$ (with $\gamma = 100$ and $l_c = 8 \text{ }\mu\text{m}$), (b1)-(b3) different beam Lorentz factors $\gamma = 50, 200$, and 250 (with $n_{b0} = 1.72 \times 10^{25} \text{ m}^{-3}$ and $l_c = 8 \text{ }\mu\text{m}$), (c1)-(c3) different average pore sizes $l_c = 4, 6$, and $10 \text{ }\mu\text{m}$ (with $\gamma = 100$ and $n_{b0} = 1.72 \times 10^{25} \text{ m}^{-3}$). Scintillation indices $\Sigma = (\langle n_b^2 \rangle / \langle n_b \rangle^2) - 1$ corresponding to the beam electron densities are presented by red curves. The SiO_2 foams in (a) and (b) are of the same initial structure.

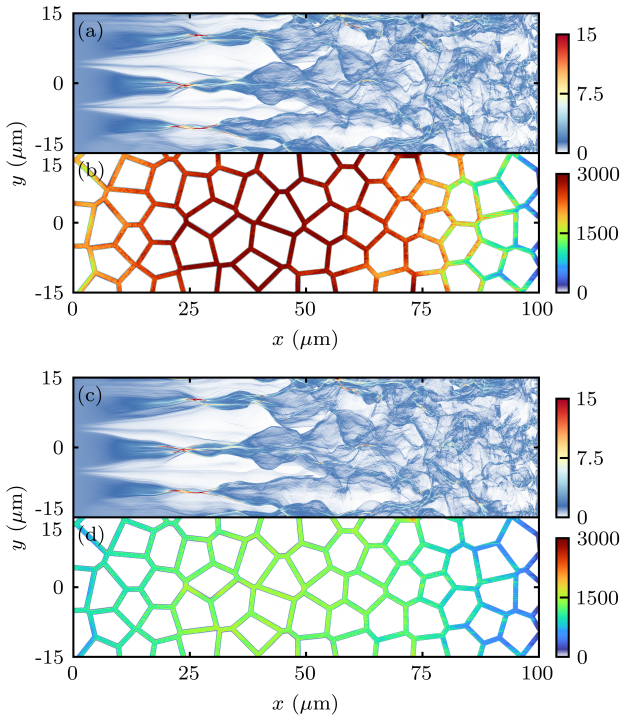


FIG. 6. (a)(c) Densities (in unites of n_{b0} , same below) of the beam electrons, (b)(d) densities of the foam electrons at $t = 333 \text{ fs}$. For (a)(b), the initial foam's Si atom density $n_{\text{Si}} = 4.3 \times 10^{27} \text{ m}^{-3}$. For (c)(d), $n_{\text{Si}} = 2.15 \times 10^{27} \text{ m}^{-3}$.

The above analysis demonstrates a linear scaling between both B_z and E_y with n_{b0} and l_c . This correlation is substantiated through a series of simulations with varied values of n_{b0} and l_c . Figures 2 and 3 illustrate the observed increase in B_z and E_y with increasing n_{b0}

and l_c . In addition, in all the cases, the distributions of pore fields are quite similar. This further validates the association of pore fields with the skeleton-and-pore microstructure, indicating that the free evolution of these fields is constrained by the latter. Figure 4 for the field strengths at the same or equivalent positions shows the linear scaling of B_z and E_y with n_{b0} and l_c , agreeing with our analysis.

IV. BRANCHED FLOW PATTERNS FOR DIFFERENT INTERACTION PARAMETERS

A. Influence of n_{b0} , γ , and l_c on the branching pattern

Since the pore fields and the associated effective potential strength V_{rms} depend on n_{b0} and l_c , the resulting branched flow patterns are affected by these interaction parameters. In addition, the Lorentz factor γ of the REB determines the dynamics of beam electrons under the pores fields, it is thus also crucial for the branched flow patterns. One can characterize the branched flow patterns by considering the distance d_0 from the foam's front surface to the first caustics, thus d_0 , in a sense, represents the transition from order to randomness. Figure 5 shows the branched flow patterns and associated variation strength of the beam density (namely, scintillation index) $\Sigma = (\langle n_b^2 \rangle / \langle n_b \rangle^2) - 1$ for different interaction parameters. It shows that d_0 decreases with increasing n_{b0} and l_c but increases with higher γ , in good agreement with Eq. (1).

As d_0 increases, we find that the branches are less likely to overlap with each other. Instead, they seem to be confined in the pores and propagate rather stably as individual strands, leading to a mild spatial evolution

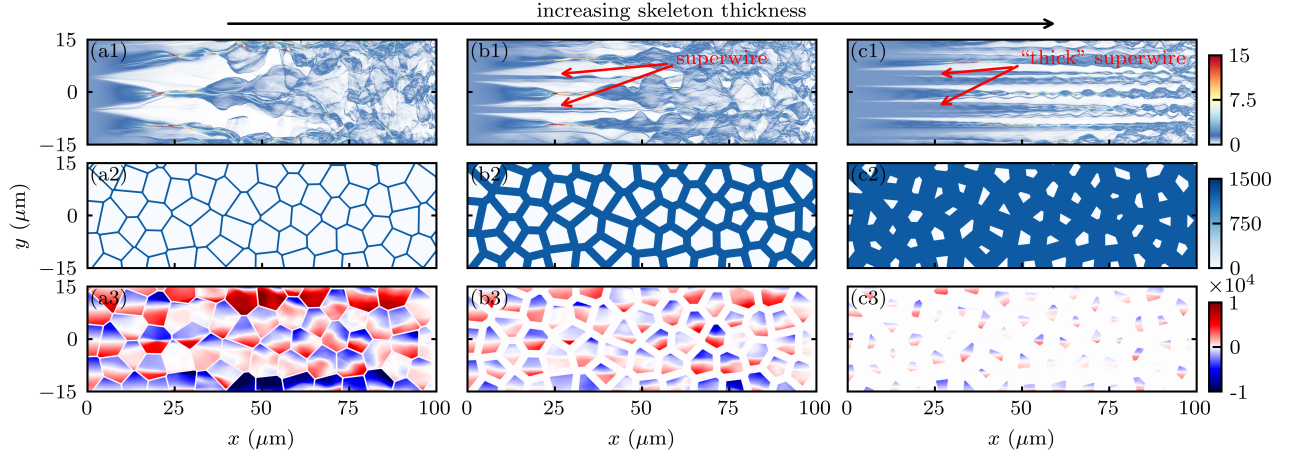


FIG. 7. From top to bottom, distributions of beam electron density (in units of n_{b0} , same below), initial foam's Si atom density, and azimuthal magnetic field B_z (in tesla). From left to right, the skeleton thickness $l_d = 0.5, 2.3$, and $4.8 \mu\text{m}$.

of Σ . This behavior can be interpreted in terms of the focusing angle θ of the REB, defined as $\tan \theta = l_c/2d_0 \propto n_{b0}^{2/3} l_c^{4/3} \gamma^{-2/3}$. We see the branches become collimated with decreasing n_{b0} and l_c , and increasing γ , which agrees with Fig. 5. Collimated branches may lead to low-divergence x - and γ -rays.

It is worth mentioning that l_c not only affects d_0 and θ , but also determines the number of the first caustics in the transverse direction. It is consistent with the universal feature of branched flows, where the average transverse separation between two adjacent caustics equals the correlation length of the effective potential¹⁻⁴ - corresponding, in our case, to l_c . As l_c approaches zero, the transverse separation between adjacent caustics tends to zero, and d_0 approaches infinity. That is, REB branching is absent in continuum media.

B. Influence of n_p and l_d on the branching pattern

Equation (1) reveals another unique feature of REB branching: the branched flow pattern is independent of the skeleton electron density n_p . This distinguishes REB branching from beam-plasma instabilities, as the latter can be sensitive to n_p ²⁸⁻³⁵. This feature of REB branching is observed under the condition that the skeleton is sufficiently dense to be considered rigid during REB propagation, i.e., $n_p \gg n_{b0}$. In this case, the pore fields and associated V_{rms} exclusively depend on n_{b0} and l_c , as discussed in Sect. III. Therefore, the dynamics of beam electrons are unaffected by n_p . Figure 6 for simulation results with different skeleton atom densities confirms that the branching patterns remain almost identical despite substantial differences in the skeleton densities.

Figure 7 illustrates the influence of skeleton thickness l_d on the branching pattern. This effect stems from our model, where V_{rms} is obtained under the assumption

that l_d approaches zero. Given that both B_z and E_y are effectively zero in the skeletons, an increase in l_d results in decreasing V_{rms} . As a result, d_0 occurs at a longer distance in dense foam with thicker skeletons. In addition, finite l_d gives rise to the formation of so-called superwires³⁶, which can propagate as stable thin filaments over extended distances, as indicated by the red arrows in Figs. 7(b1) and (c1). Superwires emerge when a certain beam electron and its neighboring ones in phase space coincidentally follow similar trajectories, maintaining stable manifolds over a finite time. As $\partial_{xx}V$ and $\partial_{yy}V$ are effectively zero in the skeletons, the stability matrix \mathcal{M} of beam electrons with similar conditions is more likely to remain stable for thick skeletons. See Ref. [37] for the definition of \mathcal{M} and detailed discussion. That is, superwires can form and propagate extensively in foams with thick skeletons.

V. FROM INDIVIDUAL BEAM ELECTRONS' PERSPECTIVE

In this section, we employ particle tracing methods to gain insights into REB branching. As shown in Fig. 8(a), the trajectories of individual electrons exhibit a quasi-ballistic nature. That is, the branched flow pattern develops linearly, allowing us to treat the beam electrons as single particles due to the absence of collective motion. Here, the term “linearly” refers to that the uneven background fields remain quasistatic during pattern formation. In this sense, one may artificially divide the REB branching into two stages. The first is a nonlinear stage of the background fields induction by the return current, as a consequence of the collective response of foam electrons to the high-current REB. The second stage appears to be linear, during which the beam electrons undergo scattering by the uneven fields, behaving as individual particles.

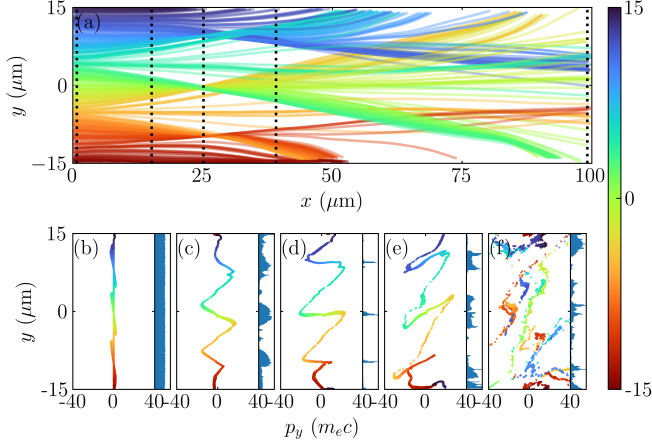


FIG. 8. (a) Trajectories of randomly selected 300 beam electrons. (b)-(f) Phase spaces (p_y, y) of randomly selected 4000 beam electrons at $x = 0.8, 15.2, 25.2, 39.2,$ and $99.2 \mu\text{m}$, respectively. The corresponding histograms are shown on the right side. The color bar is for the initial y coordinates of the selected beam electrons.

The formation of branching patterns from random scatterings is elucidating when observed in the phase space (p_y, y) of the traced beam electrons. As shown in Fig. 8(b), the initial (p_y, y) is nearly a straight line since the beam is initially monoenergetic. The corresponding beam density is also uniform, as indicated by the histogram on the right side. As the beam propagates, successive random kicks from the uneven fields cause the phase space (p_y, y) to stretch and curve, resulting in a focused beam, see Fig. 8(c). As a result, three singularities, where $\partial_y p_y = \infty$, occur around $x \sim 25 \mu\text{m}$, as shown in Fig. 8(d). These singularities in the phase space correspond to caustics, where the beam converges to an extremely high density, as shown in the histogram and Fig. 1. The phase space undergoes folding after the caustics, giving rise to individual branches in the coordinate space. For each branch, the peripheral density is higher than that at the center, see Fig. 8(e). Eventually, the phase space evolves into random distributions through further random scatterings as well as overlapping of different branches, see Fig. 8(f). Figure 8(f) also reveals an intriguing aspect of REB branching wherein groups (or manifolds) of beam electrons at neighboring initial locations can extend over significant zones over time. This emphasizes the sensitivity of a single electron's motion to its initial condition. However, the resultant branched flow pattern, formed by the ensemble of beam electrons, adheres to well-defined statistical laws²⁻⁴.

Figures 9(a)-(c) show the fields experienced by beam electrons. Indeed, in the foam target, these fields evolve randomly and are several orders of magnitude stronger than that of homogeneous targets at the same average density. Such strong and dynamic fields may lead to efficient radiation in foam targets. By analyzing the

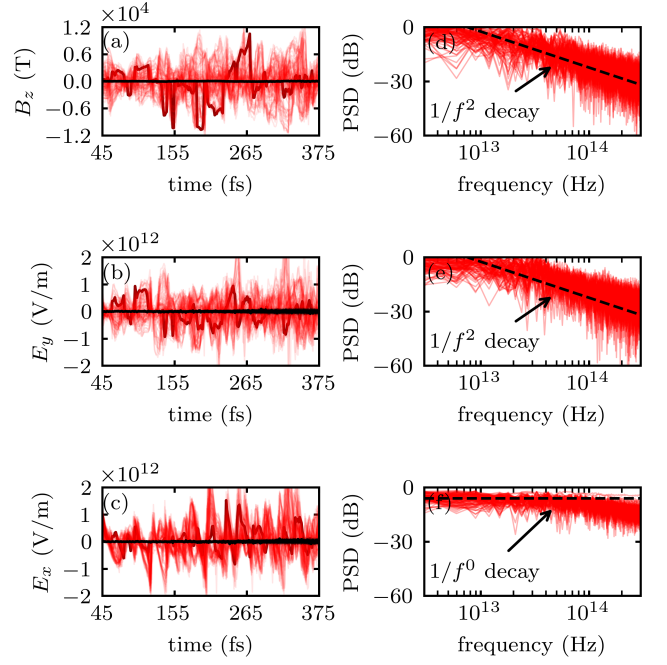


FIG. 9. Evolution of (a) azimuthal magnetic field B_z , (b) transverse, and (c) longitudinal electric field E_y and E_x experienced by randomly selected 100 beam electrons as they propagate in the foam (red) and a homogeneous target (black) at the same average density of the foam for reference. The dark red curves correspond to that experienced by a typical beam electron. (d)-(f) show the corresponding power spectral densities (PSD) of B_z , E_y , and E_x in the case of foam target, respectively.

power spectral density, defined as $\text{PSD} = \mathcal{F}(\mathcal{W})^2/C$, one sees in Figs. 9(d) and (e) that the frequency densities of B_z and E_y are inversely proportional to f^2 . It further confirms the time-correlated characteristic, akin to Brownian noise³⁸, of the transverse fields. Here, \mathcal{F} denotes to Fourier transform, \mathcal{W} is a generalized signal corresponding to the fields experienced by beam electrons in this context, C serves as a normalizing constant, and f is the frequency of \mathcal{W} . On the other hand, the frequency density of E_x appears relatively constant, namely inversely proportional to f^0 , as shown in Figs. 9(f). This suggests a negligible correlation in the longitudinal direction, resembling white noise characteristics³⁸. Therefore, even though the beam electrons experience random interactions in both longitudinal and transverse directions, branching exclusively manifests in the latter.

VI. DISCUSSION

REB branching in porous materials is a quite complicated process. This paper only addresses REBs with simplified “plane wave” profile, focusing on the impact of beam and foam parameters on the branched

flow pattern. There are other important interaction parameters. For example, REB's temporal profile is directly related to the time-dependent $n_{b0}(t)$. Therefore, the location of the first caustics can vary over time as $d_0 \propto l_c^{-1/3} n_{b0}(t)^{-2/3} \gamma^{2/3}$. In the case of a temporally Gaussian REB with sufficient duration, d_0 first decreases with time and then increases with it. The initial emittance and energy spread of REBs can also affect the resulting pattern¹¹. Moreover, foams are not necessarily isotropic, i.e., l_c can vary in different locations, modifying the correlation of induced pore fields and resulting REB dynamics.

Branched flow of REBs with unique features may open up new avenues in beam-plasma physics. Due to the pore-and-skeleton structures, the foam facilitates effective and volumetric heating¹¹, thereby attaining high-energy-density states. The heating mechanism for ions may depend on the skeleton thickness, probably transitioning from skeleton-normal sheath acceleration for thick skeletons to Coloumb explosion for thin skeletons. Moreover, there is a prospect of fabricating the foam target using nuclides of interest and harnessing the dense return current within the skeletons for nuclear excitation. In addition, REB propagation in foam experiences rapidly changing strong fields, offering promise for generating tunable bright radiations by adjusting beam and foam parameters. We believe that the journey to understanding this intriguing phenomenon has just begun.

ACKNOWLEDGEMENT

This work is supported by the National Key R&D Program of China (Grant No. 2022YFA1603300), the National Natural Science Foundation of China (Grants No. 12205201, No. 12175154, No. 12005149, and No. 11975214), the Shenzhen Science and Technology Program (Grant No. RCYX20221008092851073, 20231127181320001). The EPOCH code is used under UK EPSRC contract (No. EP/G055165/1 and No. EP/G056803/1).

DATA AVAILABILITY

The data that support the findings of this study are available from the corresponding author upon reasonable request.

REFERENCES

- ¹E. J. Heller, R. Fleischmann, and T. Kramer. Branched flow. *Physics Today* **74**, 12, 44 (2021).
- ²L. Kaplan. Statistics of branched flow in a weak correlated random potential. *Phys. Rev. Lett.* **89**, 184103 (2002).

- ³J. J. Metzger, R. Fleischmann, and T. Geisel. Universal statistics of branched flows. *Phys. Rev. Lett.* **105**, 020601 (2010).
- ⁴J. J. Metzger, R. Fleischmann, and T. Geisel. Statistics of extreme waves in random media. *Phys. Rev. Lett.* **112**, 203903 (2014).
- ⁵H. Degueldre, J. J. Metzger, T. Geisel, and R. Fleischmann. Random focusing of tsunami waves. *Nat. Phys.* **12**, 259 (2016).
- ⁶M. A. Topinka, B. J. LeRoy, R. M. Westervelt, S. E. J. Shaw, R. Fleischmann, E. J. Heller, K. D. Maranowski, and A. C. Gossard. Coherent branched flow in a two-dimensional electron gas. *Nature (London)* **410**, 183 (2001).
- ⁷A. Pidwerbetsky, Simulation and analysis of wave propagation through random media. Ph.D. thesis, Cornell University (1988).
- ⁸A. Patsyk, U. Sivan, M. Segev, and M. A. Bandres. Observation of branched flow of light. *Nature* **583**, 60 (2020).
- ⁹A. Patsyk, Y. Sharabi, U. Sivan, and M. Segev. Incoherent branched flow of light. *Phys. Rev. X* **12**, 021007 (2022).
- ¹⁰K. Jiang, T. W. Huang, C. N. Wu, M. Y. Yu, H. Zhang, S. Z. Wu, H. B. Zhuo, A. Pukhov, C. T. Zhou, and S. C. Ruan. Branched flow of intense laser light in plasma with uneven density distribution. *Matter Radiat. at Extremes* **8**, 024402 (2023).
- ¹¹K. Jiang, T. W. Huang, R. Li, M. Y. Yu, H. B. Zhuo, S. Z. Wu, C. T. Zhou, S. C. Ruan. Branching of High-Current Relativistic Electron Beam in Porous Materials. *Phys. Rev. Lett.* **130**, 185001 (2023).
- ¹²R. Jung, J. Osterholz, K. Löwenbrück, S. Kiselev, G. Pretzler, A. Pukhov, O. Willi, S. Kar, M. Borghesi, W. Nazarov, S. Karsch, R. Clarke, and D. Neely. Study of electron-beam propagation through preionized dense foam plasmas. *Phys. Rev. Lett.* **94**, 195001 (2005).
- ¹³J. Fuchs, T. E. Cowan, P. Audebert, H. Ruhl, L. Gremillet, A. Kemp, M. Allen, A. Blazevic, J.-C. Gauthier, M. Geissel, M. Hegelich, S. Karsch, P. Parks, M. Roth, Y. Sentoku, R. Stephens, and E. M. Campbell. Spatial uniformity of laser-accelerated ultrahigh-current MeV electron propagation in metals and insulators. *Phys. Rev. Lett.* **94**, 195001 (2005).
- ¹⁴M. Manclossi, J. J. Santos, D. Batani, J. Faure, A. Debayle, V. T. Tikhonchuk, and V. Malka. Study of ultraintense laser-produced fast-electron propagation and filamentation in insulator and metal foil targets by optical emission diagnostics. *Phys. Rev. Lett.* **96**, 125002 (2006).
- ¹⁵L. Romagnani, A. P. L. Robinson, R. J. Clarke, D. Doria, L. Lancia, W. Nazarov, M. M. Notley, A. Pipahl, K. Quinn, B. Ramakrishna, P. A. Wilson, J. Fuchs, O. Willi, and M. Borghesi. Dynamics of the electromagnetic fields induced by fast electron propagation in near-solid-density media. *Phys. Rev. Lett.* **122**, 025001 (2019).
- ¹⁶C. Ruyer, S. Bolaños, B. Albertazzi, S. N. Chen, P. Antici, J. Böker, V. Dervieux, L. Lancia, M. Nakatsutsumi, L. Romagnani, R. Shepherd, M. Swantusch, M. Borghesi, O. Willi, H. Pépin, M. Starodubtsev, M. Grech, C. Riconda, L. Gremillet and J. Fuchs. Growth of concomitant laser-driven collisionless and resistive electron filamentation instabilities over large spatiotemporal scales. *Nat. Phys.* **16**, 983 (2020).
- ¹⁷K. Nagai, C. S. A. Musgrave, and W. Nazarov. A review of low density porous materials used in laser plasma experiments. *Phys. Plasmas* **25**, 030501 (2018).
- ¹⁸Y. T. Li, Z. M. Sheng, Y. Y. Ma, Z. Jin, J. Zhang, Z. L. Chen, R. Kodama, T. Matsuoka, M. Tampo, K. A. Tanaka, T. Tsutsumi, T. Yabuuchi, K. Du, H. Q. Zhang, L. Zhang, and Y. J. Tang. Demonstration of bulk acceleration of ions in ultraintense laser interactions with low-density foams. *Phys. Rev. E* **72**, 066404 (2005).
- ¹⁹A. P. L. Robinson, M. H. Key, and M. Tabak. Focusing of relativistic electrons in dense plasma using a resistivity-gradient-generated magnetic switchyard. *Phys. Rev. Lett.* **108**, 125004 (2012).
- ²⁰G. Chatterjee, P. K. Singh, S. Ahmed, A. P. L. Robinson, A. D. Lad, S. Mondal, V. Narayanan, I. Srivastava, N. Koratkar, J. Pasley, A. K. Sood, and G. R. Kumar. Macroscopic transport

- of mega-ampere electron currents in aligned carbon-nanotube arrays. *Phys. Rev. Lett.* **108**, 235005 (2012).
- ²¹M. A. Belyaev, R. L. Berger, O. S. Jones, S. H. Langer, and D. A. Mariscal. Laser propagation in a subcritical foam: Ion and electron heating. *Phys. Plasmas* **25**, 123109 (2018).
- ²²T. W. Huang, C. M. Kim, C. T. Zhou, C. M. Ryu, K. Nakajima, S. C. Ruan, and C. H. Nam. Tabletop laser-driven gamma-ray source with nanostructured double-layer target. *Plasma Phys. Control. Fusion* **60**, 115006 (2018).
- ²³A. J. Kemp, S. C. Wilks, E. P. Hartouni, and G. Grim. Generating keV ion distributions for nuclear reactions at near solid-density using intense short-pulse lasers. *Nat. Commun.* **10**, 4156 (2019).
- ²⁴M. Cipriani, S. Yu. Gus'kov, F. Consoli, R. De Angelis, A. A. Rupasov, P. Andreoli, G. Cristofari, G. Di Giorgio, and M. Salvadori. Time-dependent measurement of high-power laser light reflection by low-Z foam plasma. *High Power Laser Sci. Eng* **9**, e40 (2021).
- ²⁵K. Jiang, A. Pukhov, and C. T. Zhou. TJ cm-3 high energy density plasma formation from intense laser-irradiated foam targets composed of disordered carbon nanowires. *Plasma Phys. Control. Fusion* **61**, 015014 (2021).
- ²⁶T. D. Arber, K. Bennett, C. S. Brady, A. Lawrence-Douglas, M. G. Ramsay, N. J. Sircombe, P. Gillies, R. G. Evans, H. Schmitz, A. R. Bell, and C. P. Ridgers. Contemporary particle-in-cell approach to laser-plasma modelling. *Plasma Phys. Control. Fusion* **57**, 113001 (2015).
- ²⁷Y. Z. Song, Z. H. Wang, L. M. Zhao, and J. Luo. Dynamic crushing behavior of 3D closed-cell foams based on Voronoi random model. *Mater. Des.* **31**, 4281 (2010).
- ²⁸E. S. Weibel. Spontaneously growing transverse waves in a plasma due to an anisotropic velocity distribution. *Phys. Rev. Lett.* **2**, 83 (1959).
- ²⁹K. M. Watson, S. A. Bludman, and M. N. Rosenbluth. Statistical mechanics of relativistic streams. I. *Phys. Fluids* **3**, 741 (1960).
- ³⁰R. C. Davidson. in *Handbook of Plasma Physics*, edited by M. N. Rosenbluth and R. Z. Galeev (North-Holland, Amsterdam, 1984), Vol. 2.
- ³¹L. Gremillet, G. Bonnaud, F. Amiranoff. Filamented transport of laser-generated relativistic electrons penetrating a solid target. *Phys. Plasmas* **9**, 941 (2002).
- ³²L. Gremillet, D. Bénisti, E. Lefebvre, and A. Bret. Linear and nonlinear development of oblique beam-plasma instabilities in the relativistic kinetic regime. *Phys. Plasmas* **14**, 040704 (2007).
- ³³S. I. Krasheninnikov, A. V. Kim, B. K. Frolov, and R. Stephens. Intense electron beam propagation through insulators: Ionization front structure and stability. *Phys. Plasmas* **12**, 073105 (2005).
- ³⁴A. Bret, L. Gremillet, D. Bénisti, and E. Lefebvre. Exact relativistic kinetic theory of an electron-beam-plasma system: Hierarchy of the competing modes in the system-parameter space. *Phys. Rev. Lett.* **100**, 205008 (2008).
- ³⁵A. Bret, L. Gremillet, and M. E. Dieckmann. Multidimensional electron beam-plasma instabilities in the relativistic regime. *Phys. plasmas* **17**, 120501 (2010).
- ³⁶A. Daza, E. J. Heller, A. M. Graf, and E. Räsänen. Propagation of waves in high Brillouin zones: Chaotic branched flow and stable superwires. *Proc. Natl. Acad. Sci.* **118**, e2110285118 (2021).
- ³⁷M. Mattheakis, G. P. Tsironis, E. Kaxiras. Emergence and dynamical properties of stochastic branching in the electronic flows of disordered Dirac solids. *EPL* **122**, 27003 (2018).
- ³⁸N. Ohtomo, K. Tokiwano, Y. Tanaka, A. Sumi, S. Terachi, and H. Konno. Exponential Characteristics of Power Spectral Densities Caused by Chaotic Phenomena. *J. Phys. Soc. Jpn.* **64**, 1104 (1995).